Corrosion Science (2011) 53, 9, 2803-2814

Comparison of uniform and non-uniform corrosion induced damage in reinforced concrete based on a Gaussian description of the corrosion layer

Y.X. Zhao [a], A.R. Karimi [b], H.S. Wong [b], B.Y. Hu [a], N.R. Buenfeld [b], W.L. Jin [a]

[a] Institute of Structural Engineering, Zhejiang University, Hangzhou 310058, PR China

[b] Concrete Durability Group, Imperial College London, London SW7 2AZ, UK

Abstract

A Gaussian function is proposed to describe the non-uniform spatial distribution of corrosion products as measured from chloride-exposed reinforced concrete specimens using backscattered electron imaging and image analysis. The model provides a good fit to the observed data and limited data sets reported in the literature. Subsequently it is used as an input into a finite element analysis to provide a qualitative comparison of the damage induced on concrete from idealised uniform corrosion and more realistic non-uniform corrosion. The spatial distribution of corrosion is shown to have a major impact on the propagation phase, directly influencing residual service life.

Keywords: steel reinforced concrete, SEM, modelling studies, rust

1. Introduction

Over the past several decades the corrosion of reinforcement has been identified as the main cause of deterioration in concrete structures [1]. The increased incidence of reinforcement corrosion is partly due to the more severe environmental conditions that structures are now exposed to such as the greater application of de-icing salts on bridges during winter periods and the rise in construction of new infrastructure within close proximity to coastal areas. Chloride ions are the main cause of the initiation of reinforcement corrosion and exposing concrete structures to environments rich in this ion significantly increases the risk of structural degradation. The initiation of chloride-induced reinforcement corrosion is a very complex process involving the interaction of a number of transport mechanisms and the exceedance of a chloride threshold level at the surface of the rebars [2-5].

Following the onset of corrosion, if no remedial measures are undertaken, the resulting increase in volume associated with the formation of corrosion products will exert an outward expansive pressure on the surrounding concrete eventually leading to cracking and spalling of the cover. The subsequent reduction in bond between the steel and concrete and the loss of rebar cross-sectional area will, in time, adversely affect the serviceability and load capacity of reinforced concrete elements. It is essential that the various stages of corrosion-induced damage are well understood and reliably modelled in order to enable efficient and cost-effective repair and maintenance strategies to be implemented. A comprehensive review of all possible critical limit states pertaining to the deterioration of corroding reinforced concrete

structures from initiation to collapse is presented by Buenfeld et al. [6].

The total service life of reinforced concrete elements subject to corrosion is commonly represented as a two stage process consisting of an initiation period and a propagation period [7]. The former is defined as the time taken for the onset of reinforcement corrosion and the latter is defined as the time taken to reach specified serviceability or ultimate limit states. Service life has traditionally been taken as equal to the duration of the initiation period and consequently much of the research work undertaken has been focused on this area. However this may be regarded as a too conservative failure criterion since the end of the initiation phase only signifies the onset of corrosion and the structure is yet to suffer any adverse affects that may inhibit its functional performance.

Over the past few years greater emphasis has been placed on investigating the propagation phase [8-18]. This allows for the consideration of more realistic failure criteria to signify the end of structural service life such as the initial full depth cracking of the cover, cracks exceeding a maximum allowable width, cover spalling and eventual structural collapse [19]. However the vast majority of models developed assume a uniform expansion of corrosion products around the rebar circumference [e.g. 12-18]. This is rarely the case in practice as chlorides penetrate to the depth of the reinforcement through the cover initiating corrosion on the face of the rebar closest to the concrete surface resulting in uneven distribution of corrosion products around the rebar perimeter. The assumption of uniform corrosion is made primarily for two reasons. The first is that it significantly simplifies the modelling process especially when formulating analytical and finite-difference based solution schemes. The second is that currently there is an absence of reliable information with which to characterize the actual non-uniform formation and expansion of corrosion products from the rebar surface.

Many studies have been carried on understanding the microstructure and types of corrosion products that form at the steel-concrete interface [20-25], but limited research exists on quantifying the spatial distribution of corrosion products and its effect on cover cracking. The latter point is highlighted when reviewing studies comparing corrosion-induced cover cracking arising from uniform and non-uniform corrosion propagation [e.g. 26, 27] where the investigators simply assume arbitrary elliptical shapes for the “corrosion front”.

The aim of this study is to undertake a qualitative comparison of the damage induced on the concrete cover as a result of uniform and non-uniform reinforcement corrosion based on the actual propagation of the uneven corrosion front as observed from reinforced concrete specimens corroded under simulated natural environmental conditions. The spatial distribution of the corrosion layer at the steel-concrete interface is established by imaging carefully prepared samples using a field-emission scanning electron microscope in the backscattered electron (BSE) mode. A Gaussian function is proposed to mathematically describe the measured variability in the corrosion layer and subsequently used as an input into the finite element code DIANA. Damage is modelled using the smeared-crack approach [28-31] with a linear

tension strain-softening behaviour [32]. Different stages of crack evolution ranging from its initiation at the steel-concrete interface to reaching various surface crack widths are simulated for both uniform and non-uniform corrosion and output parameters such as the maximum displacement of the corrosion front, applied expansive pressure and associated loss of steel cross-sectional area are reported and discussed. This study forms part of a larger investigation to gain deeper insight into the mechanism of corrosion propagation [33] with the ultimate aim of producing reliable service life prediction models.

2. Experimental

A summary of the experimental program is provided below. For full details of the materials, mix proportions, curing regime, exposure history and sample preparation techniques used in the study refer to Wong et al. [33].

2.1 Reinforced concrete test panels and exposure history

The investigation has been carried out on ordinary Portland cement concrete (NC) and a triple blended concrete (HPC) that contained slag and fly ash at 40 wt.% and 30 wt.% replacement levels respectively. The water/binder ratios were 0.44 for the NC and 0.345 for the HPC. The HPC contained a commercial calcium nitrite based corrosion inhibitor. The gravel and sand were siliceous aggregates at 20 mm and 5 mm maximum size respectively. The 28-day compressive strengths of NC and HPC were 50 MPa and 56 MPa respectively, as measured on 150 mm cubes.

More than one thousand reinforced concrete panels were prepared as part of a long-term research project on chloride-induced corrosion in a cyclic wet-dry environment. Each panel contained three 16 mm nominal diameter deformed (corrugated) carbon steel bars. The bars were used as-received and no efforts were made to remove existing millscale. Some panels were cast with a cover depth of 20 mm as shown in Figure 1, others with a cover depth of 40 mm.

The panels were subjected to alternate wetting and drying cycles in an environmental chamber to induce corrosion. The side and bottom surfaces of each panel were surface treated with epoxy resin and a polyurethane coating to ensure that chloride predominantly penetrated through the top cover. Each wet/dry cycle lasted for 3 days and consisted of spraying 3.53 wt.% NaCl solution for 4 hours and subsequent drying at 40 °C for the remaining period. After approximately 12 months of exposure, a small number of panels (those with a low cover depth of 20 mm) exhibited signs of corrosion damage. Therefore, only two such panels, one from each mix, were subsequently removed from the environmental chamber for further testing. Panels with 40 mm cover depth showed no surface signs of corrosion damage at this stage and were kept within the environmental chamber for testing at a later date to provide a comparison with the results obtained in this investigation.

2.2 Sample preparation for microscopy

The selected panels were carefully cut with a diamond saw to extract the corner and middle rebars, with their surrounding concrete intact as shown in Figure 2. Sectioning was done at least 15 mm away from the rebar to minimise any disturbance to the rebar-concrete interface. The sectioned panels were labelled as NC-A, NC-B and HPC-A, where A and B represent the sections containing the corner and middle rebars respectively. The middle rebar of the HPC panel was not further tested since it was unaffected by corrosion. The sectioned panels were dried at 50 ˚C and subsequently cast in a low viscosity epoxy which was allowed to harden for several days.

Each section was then cut sequentially starting from the side face to produce a series of 8 mm-thick cross-section slices. A total of fifty-seven slices were produced. An example of a slice is shown in Figure 3a. The overall process of preparing a given slice for microscopic examination and measuring the corrosion layer thickness around the whole perimeter of a rebar is very labour intensive and time consuming. Therefore it was decided for this first study to limit the selection to five slices that exhibit varying degrees of reinforcement corrosion, covering a range of corrosion layer topography and corrosion-induced damage. The locations of these slices within their respective panels are indicated in Figure 2, for example, 'NC-A-10' represents a slice at 10 mm from the side face of panel NC containing a corner rebar. To produce samples for microscopy, the slices were vacuum-impregnated with a low viscosity epoxy, trimmed down to 50 × 25 × 8 mm blocks and then ground with SiC papers at 500, 1000 and 1200 grit to expose a fresh surface. The blocks were then polished using diamond with successively finer grit size down to a 0.25 μm finish.

2.3 Backscattered electron imaging

A field-emission scanning electron microscope in the backscattered electron (BSE) mode was used for measuring the thickness of the corrosion layer. The microscope was operated at 10 kV accelerating voltage, 10 mm working distance and under low vacuum conditions. In a BSE image, the boundaries of the rebar, corrosion layer and cement paste are clearly visible due to large differences in their mean atomic numbers (Figure 3b). This enables accurate measurements of the corrosion layer thickness to be made. For each polished block, measurements were made on at least 60 locations around the perimeter of the rebar, by moving the sample using a motorised stage with a precision of 0.5 μm in the *x* and *y*-direction. The spatial coordinates of every measurement location were noted. In some locations, corrosion products may have migrated into the cement paste via pores and cracks [33], but these were not considered in the measurement.

3. Corrosion-damage model

The finite element code DIANA is utilized to model corrosion-induced crack initiation and propagation. The problem is idealized in two-dimensions with the finite element discretization of a reinforced concrete panel cross-section as shown in Figure 4. Concrete is assumed to be a homogenous material and modelled using eight-node quadrilateral

isoparametric elements with a fine mesh size in close proximity to the reinforcing bars which is relaxed to a coarser mesh with distance away from the reinforcement for the sake of computational efficiency. Displacements along the *x* and *y*-axes are restrained at the bottom surface of the member cross-section. The smeared crack approach is implemented to model concrete cracking with the analysis performed under the assumption of plane strain. The material properties assumed for NC and HPC are presented in Table 1. The modulus of elasticity of the concrete E_c and its uniaxial tensile strength f_t are evaluated from the measured compressive cube strength in accordance with the Chinese concrete code [34]. The fracture energy of concrete G_F is estimated based on its compressive strength and the maximum aggregate size as directed by the CEB-FIP model code [35]. The concrete material model, failure criterion and simulation of reinforcement corrosion are discussed below.

3.1 Concrete material model

The constitutive model for concrete in tension is shown in Figure 5. Prior to cracking a linear stress-strain relationship up to a limiting tensile stress f_t is specified as shown in Figure 5a. Subsequent to crack formation the concrete tension softening in a direction normal to the crack is represented in terms of a linear stress σ_t versus crack opening displacement *w* relationship as shown in Figure 5b. The tensile stress decreases to zero at the critical displacement w_c which is the crack opening displacement associated with the traction-free (i.e. no friction between the opposing surfaces of the crack) condition. The area under the tension softening curve is equal to the fracture energy G_F, defined as the energy required to propagate a unit area of traction-free crack.

The limiting tensile stress f_t at which cracks initiate is set equal to the uniaxial concrete tensile strength. A more rigorous approach would be to base the maximum permissible tensile stress f_t on a biaxial stress state where f_t can be specified as a function of applied compressive stresses along a perpendicular axis. However when analysing concrete behaviour under corrosion-induced stresses alone, the magnitude of induced compressive and tensile stresses are typically of the same order of magnitude. Under such conditions the concrete tension fracture criterion is not appreciably affected and the failure surface can be suitably represented by the uniaxial tensile strength. It also follows on from this discussion that the compressive behaviour of concrete will have little impact on the output of the analyses. Therefore concrete is assumed to behave as an ideal elastic perfectly plastic material in compression with failure defined by the Drucker-Prager failure surface.

3.2 Simulation of reinforcement corrosion

To simulate the expansive formation of corrosion products, nodal displacements are imposed at the steel-concrete interface in the finite element model. The initial undamaged rebar is transformed by applying a large number of very

small radial increments. The loading process is continued until the required degree of damage is inflicted on the concrete member or the numerical solution fails to converge. Only one corner reinforcing bar is subjected to corrosion in line with the corrosion state observed in the HPC panel.

Three separate corrosion schemes are considered, one representing uniform corrosion and the remaining two non-uniform corrosion as shown in Figure 6. The non-uniform corrosion states correspond to cases where only a segment of the rebar circumference is corroding and where corrosion is occurring unevenly around the whole circumference of the rebar. These are designated as scenarios (i) and (ii) respectively and are described in Table 2. The corrosion fronts specified in the analysis at each increment step are evaluated from Equation 1 which is derived based on the actual measured corrosion layer thickness T_r around a rebar as detailed in section (4.2). Taking T_r to be the final geometry of the corrosion layer and defining α as the load coefficient, at each increment a displacement of αT_r is imposed on the nodes at the steel-concrete interface. To facilitate a stable transfer of load onto the concrete boundary, α for the first load increment is set to a very small value of 1×10^{-5}. Subsequently as the loading progresses the coefficient α is automatically adjusted by the software according to the outcome of the previous load step.

4. Results

4.1 Overview of samples

The five samples selected for this study exhibit varying degrees of corrosion and cracking. The amount of corrosion, defined as the measured area of corrosion products expressed as percentage of the original rebar cross-sectional area, ranges from 3 % to 9 %. The amount of damage, defined as the measured area of cracks expressed as percentage of the original rebar cross-sectional area, ranges from about 2.5 % to 14 %. As expected the amount of damage increases with corrosion degree. A detailed study of the amount of corrosion and induced damage, their variation along the length of the panels and the microstructure of the corroded interface including the distribution and extent of corrosion products penetration into the cement paste is reported in an earlier paper [33].

Corrosion is more severe on slices taken near the side face compared to those farther away. Slices from the corner rebar are slightly more damaged compared to those from the middle rebar, given the same amount of corrosion. It is clear that the amount of corrosion products at the rebar-concrete interface is not uniform around the rebar, but accumulates mainly in the upper half, where it is closest to the exposed top cover as can be seen in Figure 3a. Most cracks near the rebar-concrete interface are filled with corrosion products or have surfaces lined with corrosion products. In all slices affected by corrosion, there is at least one major crack from the rebar through the full depth of the top cover. The widths of the surface cracks measured on the top cover range from 0.05 to 0.9 mm.

4.2 Corrosion layer thickness

Figure 7 shows the variation in the measured corrosion layer thickness around the rebar circumference for the five selected samples. The results are plotted against polar coordinates where the origin ($\theta = 0$) is defined according to the schematic shown in Figure 8 for the corner and middle rebars. The results show a large scatter in measured thickness, but some trends are apparent. As the sample becomes more corroded, the spread and thickness of the corrosion layer increases. The largest recorded thickness is approximately 1 mm. For the corner rebars, the maximum thickness occurs at around $\theta = \pi$, while for the middle rebars, the location of the maximum thickness is slightly shifted from $\theta = \pi$.

The data was fitted using several equations and it was found that an equation based on a Gaussian function is suitable to describe the corrosion layer thickness around the rebar for the case of non-uniform corrosion:

$$T_r = \frac{a_1}{a_2 \cdot \sqrt{2\pi}} \cdot e^{-\left(\frac{\theta - a_3}{\sqrt{2}a_2}\right)^2} + T_0 \qquad (1)$$

Where T_r is the thickness of corrosion layer at coordinate θ and a_1, a_2, a_3 and T_0 are fitting parameters. The values of a_1, a_2, a_3 and T_0 from the regression analysis are presented in Table 3. The regression line for each sample and its corresponding 95 % confidence intervals are also plotted in Figure 7. The parameters a_1, a_2, a_3 and T_0 describe various characteristics of the fitted curve. For example, a_1 and a_2 correlate to the maximum thickness and the spread of the corrosion layer respectively. Parameter a_3 is the polar coordinate of the peak, i.e. where maximum corrosion thickness occurs and parameter T_0 defines the minimum thickness of the corrosion layer. It should also be noted that T_0 is the thickness of the corrosion layer for the case when corrosion occurs uniformly around the rebar, i.e. when $a_1 = 0$.

The above equation can be used to describe two general corrosion scenarios as shown in Table 2. In the first scenario, the corrosion layer covers only a portion of the rebar circumference, hence $T_0 \sim 0$, for example in NC-B-20 and NC-B-30. The second scenario describes a more severe corrosion, where the corrosion layer is fully developed across the entire circumference of the rebar, for example in samples HPC-A-20, HPC-A-30 and NC-A-10. The parameters a_1, a_2 and a_3 can also be determined analytically by substituting the boundary conditions given in Table 2 into Equations 2 or 3 for the governing corrosion scenario. However, the required boundary conditions necessitate measurements to be made on the corroded steel-concrete interface, which is difficult to achieve in practice. Table 3 provides the analytically derived coefficients and it can be observed that the results correlate well with the regression values.

As can be seen from Figure 7, the proposed Gaussian model provides a good fit to the measured variation of the corrosion layer thickness around the perimeter of the five rebars examined. To further test the validity of the approach, additional data on the uneven distribution of corrosion products around a rebar as provided by Yuan and Ji [36] is analyzed. Yuan and Ji exposed concrete samples containing 14 mm diameter plain rebars to varying aggressive

environments and subsequently measured the thickness of the non-uniform corrosion layer formed for three samples designated as Y&J 1 to 3. Corrosion-induced cover cracking was only evident on sample Y&J 3, the other two samples remaining uncracked. The regression analysis of the proposed Gaussian model on the reported data points, the associated 95 % confidence intervals on the regression lines and the analytically derived corrosion layer thickness based on the observed boundary conditions are shown in Figure 9. The corresponding values of the model coefficients are tabulated in Table 4. Again it is clear that the model provides a good fit to the experimentally obtained corrosion layer thickness.

It is acknowledged that the Gaussian model has been established based on only 8 samples. The results from this work are valid for these samples investigated and may not be suitable for other situations. Obviously to develop a model for the absolute thickness of the corrosion layer much more work needs to be done, for example measuring the variation in corrosion layer thickness for different type specimens to consider the effects of exposure environments, time and rebar location, which influence the parameters a_1, a_2, a_3 and T_0 in Equations 2 and 3. This constitutes the next phase of the research program where numerous panels from those currently in storage within the environmental chamber will be removed and subjected to the same examination procedure. Nevertheless it is recommended that investigators studying the damage induced by non-uniform reinforcement corrosion on concrete utilize the Gaussian description of the corrosion layer as formulated by the authors in preference to assuming arbitrary elliptical representations of the corrosion front.

4.3 Analysis of uniform and non-uniform corrosion

As described in section (3.2) three corrosion regimes are considered, one uniform and two non-uniform corrosion cases defined as scenarios (i) and (ii) (see Table 2 for details). Corrosion is propagated to attain four specified stages of damage. These are stages (1) and (2) which represent first crack initiation at the steel-concrete interface and outer surface of the concrete respectively, and stages (3) and (4) when the maximum surface crack width has reached a magnitude of 0.01 and 0.05 mm respectively. For stages (1) and (2) cracks are initiated when the permissible tensile strength of concrete f_t is exceeded. The crack width of 0.01 mm specified at stage (3) corresponds to the fracture of concrete and formation of micro-cracks within the fracture process zone (FPZ). The crack width of 0.05 mm specified at stage (4) corresponds to the first visible surface cracks as observed through a magnifying glass in accelerated corrosion tests on reinforced concrete specimens [37]. Damage states above a crack width of 0.05 mm are not included in the study due to the failure of the numerical solution to converge. Therefore the unstable propagation of macro-cracks under constant load which occurs at advanced stages of damage and the associated localization of strain within the FPZ resulting in the arrest or even closure of micro-cracks outside the FPZ are not considered. The analyses are undertaken based on the material properties of both NC and HPC as tabulated in Table 1. For scenarios (i) and (ii) the outer

perimeter of the corrosion layer is represented using Equations 2 and 3 respectively with the regression parameter values derived from samples NC-B-30 and HPC-A-20 (see Table 3).

The results of the analysis are presented in Figures 10 to 15 and cover a range of variables of interest at each stage of damage including the maximum imposed radial displacement at the steel-concrete interface, loss of rebar area and variation in the applied pressure distribution around the reinforcement perimeter. The predicted formation of crack patterns is also shown. In general the difference in model outputs between NC and HPC is small as they share similar measured compressive strengths. Therefore not all the results pertaining to each corrosion regime and damage stage are presented, but rather a selection of outcomes that best highlight the overall trends and main inferences arising from the analysis.

In some cases the model outputs are not available as the numerical solution fails to converge. This occurs at damage stage (4) for scenario (i) for both the NC and HPC analyses and for scenario (ii) for the NC analysis. At stage (4) the concrete model is extensively cracked and further loading of the concrete results in computational difficulties leading to the lack of convergence. Additionally it must be noted that due to the localized nodal displacements associated with scenario (i), computational difficulties are encountered following crack initiation at the steel-concrete interface. Therefore to attain damage stages (2) and (3) the convergence tolerance criterion is relaxed to allow the analysis to proceed. This relaxation of convergence criterion introduces greater accumulated errors in the outputs reported and therefore the results obtained for damage stages (2) and (3) for scenario (i) may not be reliable.

5. Discussion

Figure 10 presents the maximum imposed radial displacements δ_{max} as measured from the original perimeter of the uncorroded rebar at each damage stage for NC and HPC and the three corrosion regimes considered. Uniform corrosion requires the least outward expansion to reach any of the damage stages. Scenario (i) registers the highest δ_{max} at each stage as may be expected due to the localized nature of the corrosion.

Figure 11 estimates the corresponding loss in steel cross-sectional area ρ at each damage stage for NC and HPC. The steel loss ρ is defined as a percentage loss of the corroded area of the rebar over its original intact area and is calculated assuming a volumetric expansion ratio of corrosion products to the parent metal of 2. This can vary significantly ranging from as low as 2 to as high as 6 [12]. The actual value in this case is not known. However different assumed expansion ratios do not affect the relative relationships presented in Figure 11 between the three corrosion scenarios and hence have no influence on the trends observed. In comparison to scenario (ii), uniform corrosion requires a greater loss of steel area to reach the damage stages. Therefore for a given rate of corrosion scenario (ii) will induce cracks and reach limiting cracks widths at earlier times in the service life of a corroding member.

For the initiation of cracks at the steel-concrete interface scenario (i) requires the least loss of steel area. Subsequently scenario (i) experiences the greatest area losses to reach damage stages (2) and above. However due to the numerical errors associated with the analysis of scenario (i) at damage stages (2) and (3) as noted in section (4.3), it is not possible to arrive at a confident interpretation of the latter results.

Comparing the NC and HPC responses, there is generally little difference between the two cases as they have similar material properties. HPC consistently posts slightly higher values of δ_{max} and ρ as would be expected. The one major exception being at damage stage (3) of scenario (i) where both δ_{max} and ρ experience a notable increase in value when going from NC to HPC. Again it is currently uncertain whether this is an actual physical phenomenon or an artificial artefact arising from numerical errors associated with the analysis of scenario (i), damage stage (3).

The spatial variation in the magnitude of the applied expansive pressure around the perimeter of the rebar for all damage stages of the HPC panel is shown in Figure 12 for the corrosion regimes considered. The locations of the maximum applied pressures do not coincide for the three corrosion schemes. Scenario (i) experiences peak pressures over a much more localized region than the other two corrosion regimes as expected. Scenario (ii) seems to follow a similar trend in the spatial evolution of the expansive pressure as that of uniform corrosion, but at lower magnitudes on average. The maximum pressure of 37.1 MPa is recorded for the case of uniform corrosion at stage (4) of damage.

It is worth noting that the spatial build-up of pressure is not solely a function of the imposed nodal displacements, but is also influenced by the boundary constraints provided by the surrounding concrete. This can be seen in Figure 13 from the pressure distributions around the rebar for the NC panel at stage (1) of damage for uniform corrosion and scenario (i). For uniform corrosion the nodal displacements are equal all around the reinforcement yet the applied pressure distribution is non-uniform. In this case the spatial pressure variation is governed by the prevailing boundary conditions with the regions closest to the external surfaces experiencing lower pressures due to the reduced stiffness of the concrete cover. For scenario (i) the nodal displacements are concentrated over a small region of the reinforcement and therefore their action dominates over any influence exerted by the surrounding boundary constraints.

Figure 12 shows that as the severity of the induced damage increases, uniform corrosion and scenario (ii) exhibit a build-up of pressure at some locations accompanied by a relaxation of pressure at others. This relief in applied pressure is very notable in scenario (i) when comparing results obtained at damage stages (2) and (3). The observed pressure relief occurs subsequent to the initial full depth cracking of the cover when a degree of confinement provided to the rebar by the surrounding concrete is lost.

This phenomenon is more clearly illustrated by Figures 14 and 15 which trace the evolution of the crack pattern and the expansive pressure around the reinforcement as corrosion propagates in the HPC panel for scenario (ii). The crack

patterns indicated in Figure 14 are represented by lines of crack strain whose lengths are a function of applied strains and form in a direction perpendicular to the principal tensile stress. At stage (1) when cracks are just initiated at the steel-concrete interface the pressure around the rebar is reasonably uniform. The first signs of pressure relief occur at stage (2) when the cover is fully cracked resulting in some loss of bar confinement. Subsequently, as the crack network develops and becomes more extensive during damage stages (3) and (4), this loss of pressure is amplified with the pressure ultimately reaching zero in some locations. At damage stage (4) the extent of cover cracking is so great that a possible fracture plane is developing which may eventually lead to the spalling of the corner cover region A. This loss of stiffness over region A correlates well with the areas where the pressure relief is observed. In contrast, region B is located away from the outer surfaces and within the main body of the concrete section and is yet to experience a notable drop in stiffness. Therefore the applied expansive pressures around the rebar continue to build-up over this region as corrosion proceeds.

The crack pattern shown in Figure 14 for damage stage (4) consists of a network of fine cracks densely concentrated over the damaged regions. Such a predicted crack pattern is obtained due to the idealization of concrete as a homogenous material in the finite element model. In reality these fine cracks will usually coalesce into fewer but wider cracks which follow a highly tortuous path around the aggregate particles within the cement matrix.

The analysis highlights the important practical implications of uniform and non-uniform corrosion on the performance of corroding reinforced concrete elements. The form of corrosion incurred dictates the magnitude and spatial distribution of the expansive pressure applied as well as the loss of steel cross-sectional area required to reach specified damage states. The latter is of critical importance when attempting to estimate the residual service life of a deteriorating element. The research undertaken in this paper is more qualitative rather than quantitative in nature and further work is necessary to improve the accuracy of the finite element model by overcoming the numerical difficulties encountered and also by including additional governing actions such as the simultaneous corrosion of two or more bars, the confinement provided by the presence of shear links and stress fields generated by imposed loading.

6. Conclusions

Chloride-induced reinforcement corrosion leads to the non-uniform distribution of corrosion products around the rebar perimeter. So far there has been very limited information available in the literature which adequately captures the non-symmetric deposition of corrosion products thereby resulting in arbitrarily assumed elliptical boundaries for the corrosion layer by investigators studying the impact of non-uniform corrosion on concrete. This paper reports the spatial variability in the thickness of the corrosion layer around five rebars as reliably measured by undertaking high resolution image analyses of the steel-concrete interface extracted from reinforced concrete specimens corroded under simulated natural exposure conditions. A Gaussian model has been formulated to describe the phenomenon and it is shown that it

provides a good fit to the experimentally obtained results. The suitability of the model has been further tested against three additional data sets reported in the literature and a good correlation between the model and experimental results is observed.

Subsequently the Gaussian model has been used as an input into a finite element analysis comparing the damage induced on concrete from uniform and non-uniform corrosion. It is shown that the form of corrosion incurred can have a significant impact on the propagation phase and affects the build-up of expansive pressure around the rebar circumference. More critically it governs the amount of corrosion products required to reach specified stages of damage, in some cases non-uniform corrosion requiring less loss of steel area and hence a shorter propagation period to violate set performance limit states.

Acknowledgements

We acknowledge the financial support provided by the Engineering and Physical Sciences Research Council, UK and the National Natural Science Foundation of China with Grant No. 50808157 and No. 50920105806. We thank Mr. Andrew Morris for his help in preparing the samples for microscopy work.

References

[1] P.B. Bamforth, Enhancing reinforced concrete durability: guidance on selecting measures for minimizing the risk of corrosion of reinforcement in concrete, Concrete Society Technical Report No. 61 (2004).

[2] Z.P. Bazant, Physical model for steel corrosion in concrete sea structures – theory, J. Struct. Div, ASCE, 105 (1979) 1137-1153.

[3] C.L. Page, K.W.J. Treadaway, Aspects of the electrochemistry of steel in concrete, Nature 297 (1982) 109-115.

[4] G.K. Glass, N.R. Buenfeld, The presentation of the chloride threshold level for corrosion of steel in concrete, Corros. Sci. 39 (1997) 1001-1013.

[5] G.K. Glass, N.R. Buenfeld, Chloride-induced corrosion of steel in concrete, Prog. Struct. Engng. Mater. 2 (2000) 448-458.

[6] N.R. Buenfeld, R. Davies, A.R. Karimi, A. Gilbertson, Intelligent monitoring of concrete structures, CIRIA Report C661, CIRIA, London (2008).

[7] K. Tuutti, Corrosion of steel in concrete, Swedish Cement and Concrete Research Institute, Fo 4.82, Stockholm (1982).

[8] C. Alonso, C. Andrade, J. Rodriguez, J.M. Diez, Factors controlling cracking of concrete affected by reinforcement

corrosion, Mater. Struct. 31 (1998) 435-441.

[9] T. Vidal, A. Castel, R. Francois, Analyzing crack width to predict corrosion in reinforced concrete, Cem. Concr. Res. 34 (2004) 165-174.

[10] R. Zhang, A. Castel, R. Francois, Concrete cover cracking with reinforcement corrosion of RC beam during chloride-induced corrosion process, Cem. Concr. Res. 40 (2010) 415-425.

[11] C. Lu, W. Jin, R. Liu., Reinforcement corrosion-induced cover cracking and its time prediction for reinforced concrete structures, Corros. Sci. 53 (2011) 1337-1347.

[12] Y. Liu, R.E. Weyers, Modeling the time-to-corrosion cracking in chloride contaminated reinforced concrete structures, ACI Mater. J. 95 (1998) 675-681.

[13] S.J. Pantazopoulou, K.D. Papoulia, Modeling cover-cracking due to reinforcement corrosion in RC structures, J. Eng. Mech. 127 (2001) 342-351.

[14] K. Bhargava, Y. Mori, A.K. Ghosh, S. Ramanujam, Analytical model of corrosion-induced cracking of concrete considering the stiffness of reinforcement, Struct. Eng. Mech. 16 (2003) 749-769.

[15] C.Q. Li, R.E. Melchers, J.J. Zheng, Analytical model for corrosion-induced crack width in reinforced concrete structures, ACI Struct. J. 103 (2006) 479-487.

[16] S.F.U. Ahmed, M. Maalej, H. Mihashi, Cover cracking of reinforced concrete beams due to corrosion of steel, ACI Mater. J. 104 (2007) 153-161.

[17] D. Chen, S. Mahadevan, Chloride-induced reinforcement corrosion and concrete cracking simulation, Cem. Concr. Res. 30 (2008) 227-238.

[18] D.V. Val, L. Chernin, M.G. Stewart, Experimental and numerical investigation of corrosion-induced cover cracking in reinforced concrete structures, J. Struct. Eng. 135 (2009) 376-385.

[19] DuraCrete – probabilistic performance based durability design of concrete structures, Brite EuRam III, Project BE95-1347, Document BE95-1347/R17 (2000).

[20] F.P. Glasser, K.K. Sagoe-Crentsil, Steel in concrete: Part II Electron microscopy analysis, Mag. Concr. Res. 41 (1989) 213-220.

[21] K. Suda, S. Misra, K. Motohashi, Corrosion products of reinforcing bars embedded in concrete, Corros. Sci. 35 (1993) 1543-1549.

[22] A.G. Constantinou, K.L. Scrivener, Microstructural examination of the development of corrosion in reinforced

concrete, In: Mechanisms of chemical degradation of cement-based systems, in: K.L. Scrivener, J.F. Young (Eds.), E & FN Spon, London (1995) 134-142.

[23] A.K. Aligizaki, M.R. de Rooij, D.D. Macdonald, Analysis of iron oxides accumulating at the interface between aggregates and cement paste, Cem. Concr. Res. 30 (2000) 1941-1945.

[24] G.S. Duffó, W. Morris, I. Raspini, C. Saragovi, A study of steel rebars embedded in concrete during 65 years, Corros. Sci. 46 (2004) 2143-2157.

[25] W.J. Chitty, P. Dillmann, V. L'Hostis, C. Lombard, Long-term corrosion resistance of metallic reinforcements in concrete – a study of corrosion mechanisms based on archaeological artefacts, Corros. Sci. 47 (2005) 1555-1581.

[26] Y.G. Du, A.H.C. Chan, L.A. Clark, Finite element analysis of the effects of radial expansion of corroded reinforcement, Comput. Struct. 84 (2006) 917-929.

[27] B.S. Jang, B.H. Oh, Effects of non-uniform corrosion on the cracking and service life of reinforced concrete structures, Cem. Concr. Res. 40 (2010) 1441-1450.

[28] Y.R. Rashid, Ultimate strength analysis of prestressed concrete pressure vessels, Nucl. Eng. Des. 7 (1968) 334-344.

[29] Z.P. Bazant, Instability, ductility and size effect in strain-softening concrete, J. Engng Mech. ASCE 105 (1976) 331-344.

[30] Z.P. Bazant, B.H. Oh, Crack band theory for fracture of concrete, Mater. Struct. 16 (1983) 155-177.

[31] J.G. Rots, P. Nauta, G.M.A. Kusters, J. Blaauwendraad, Smeared crack approach and fracture localization in concrete, Heron, 30 (1985) 1-48.

[32] A. Hillerborg, M. Modeer, P.E. Petersson, Analysis of crack formation and crack growth in concrete by means of fracture mechanics and finite elements, Cem. Concr. Res. 6 (1976) 773-782.

[33] H.S. Wong, Y.X. Zhao, A.R. Karimi, N.R. Buenfeld, W.L. Jin, On the penetration of corrosion products from reinforcing steel into concrete due to chloride-induced corrosion, Corros. Sci. 52 (2010) 2469-2480.

[34] P R China national standards: Code for design of concrete structures (GB50010-2010).2010:16-18.

[35] Comite Euro-International du Beton – Federation Internationale de la Precontrainte, CEB-FIP Model Code, Thomas Telford Ltd, London (1990).

[36] Y.S. Yuan, Y.S. Ji., Models of corrosion distribution on steel bar in concrete under climate environment and chloride attack, Advance in Concrete Structural Durability – Proceeding of International Conference on Durability of Concrete Structures, Hangzhou, China (2008) 936-941.

[37] K. Vu, M.G. Stewart, J. Mullard, Corrosion-induced cracking: Experimental data and predictive models, ACI Struct. J. 102 (2005) 719-726.

Table 1: Material properties for NC and HPC panels.

Panel	E_c (MPa)	ν	f_t (MPa)	G_F (N/mm)
NC	34500	0.2	2.64	0.079
HPC	35500	0.2	2.74	0.086

Table 2: Description of two non-uniform corrosion scenarios.

	Scenario (i)	Scenario (ii)
	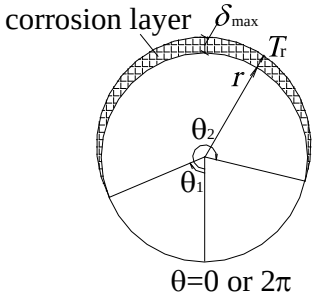	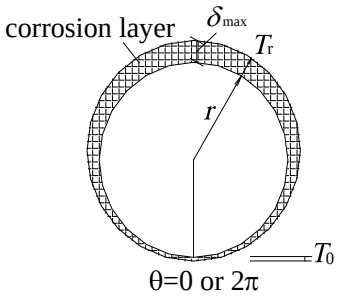
Proposed analytical model	$T_r = \frac{a_1}{a_2 \cdot \sqrt{2\pi}} \cdot e^{-(\frac{\theta - a_3}{\sqrt{2} a_2})^2}$ (2)	$T_r = \frac{a_1}{a_2 \cdot \sqrt{2\pi}} \cdot e^{-(\frac{\theta - a_3}{\sqrt{2} a_2})^2} + T_0$ (3)
	Where T_r is the thickness of the corrosion layer, θ is the polar coordinate, T_0 is the minimum corrosion layer thickness, and a_1, a_2 and a_3 are fitting coefficients.	
Boundary conditions	1. $T_r \cong 0$, $\theta = \theta_1$; 2. $T_r \cong 0$, $\theta = \theta_2$; 3. $\int_{\theta_1}^{\theta_2} T_r \mathbf{d}(\theta \cdot r) = A_r$	1. $T_r \cong T_0$, $\theta = 0$; 2. $T_r \cong T_0$, $\theta = 2\pi$; 3. $\int_0^{2\pi} T_r \mathbf{d}(\theta \cdot r) = A_r$
	Where r is the radius of rebar and A_r is the total area of the corrosion layer.	

Table 3: Values of a_1, a_2, a_3 and T_0 obtained from fitting of experimental data .

Sample	Corrosion (%)	Damage (%)	Regression				Analytically derived			
			a_1	a_2	a_3	T_0	a_1	a_2	a_3	Boundary conditions
HPC-A-20	8.99	9.00	1.583	0.895	3.224	0.135	1.537	0.867	3.142	T_o=0.135mm, A_r=18.53mm^2
HPC-A-30	6.65	7.53	1.069	0.731	3.287	0.135	1.056	0.896	3.142	T_o=0.135mm, A_r=14.83mm^2
NC-B-20	4.61	5.76	0.796	0.443	2.853	0.03	0.835	0.572	2.824	θ_1=0.78, θ_2=4.86, A_r=7.83mm^2
NC-B-30	2.97	2.61	0.151	0.382	3.726	0.03	0.168	0.309	3.648	θ_1=2.63, θ_2=4.66, A_r=1.79mm^2

NC-A-10	8.47	13.81	2.044	1.032	3.326	0.20	1.752	0.858	3.142	T_o=0.20mm, A_r=22.02mm^2

Table4: Values of a_1, a_2, a_3 and T_0 obtained from experimental data of Yuan and Ji

sample	Corrosion (%)	regression			
		a_1	a_2	a_3	T_0
Y&J 1	0.75	0.29314	0.55996	3.178	0.006
Y&J 2	0.46	0.1606	0.7053	3.312	0.006
Y&J 3	2.15	0.50572	1.19081	3.157	0.070

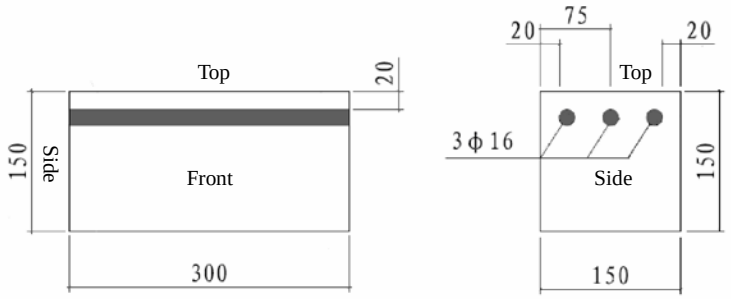

Figure 1: Schematic of the reinforced concrete panel showing the rebar arrangement (dimensions are in mm).

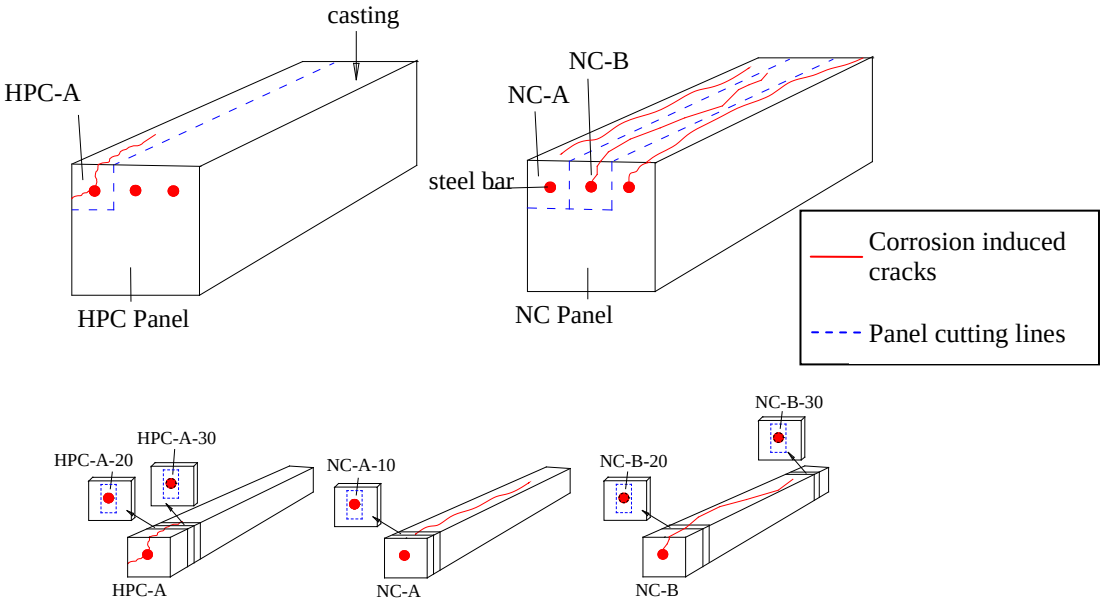

Figure 2: Schematics showing the sectioned concrete panels and locations of the 8mm thick slices.

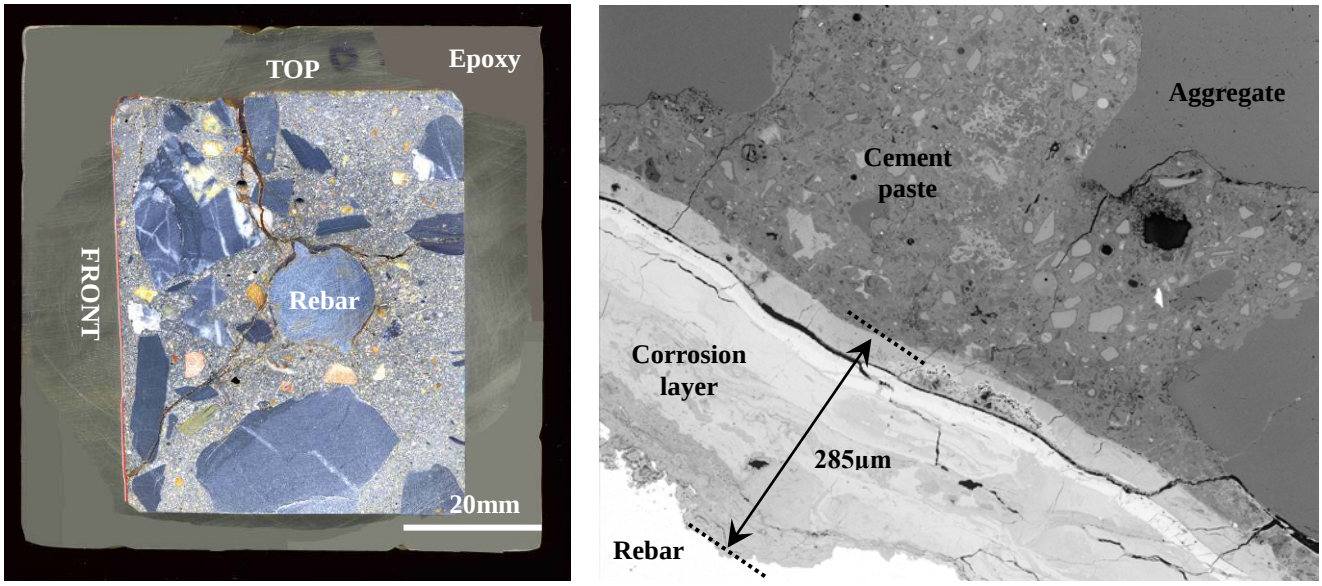

(a) (b)

Figure 3: a) Scanned image of an 8mm thick slice (NC-A-10) obtained using a flatbed scanner, and b) Backscattered electron image of a polished block sample showing accumulation of corrosion products at the rebar-concrete interface (150x magnification, field of view: 800 x 640µm).

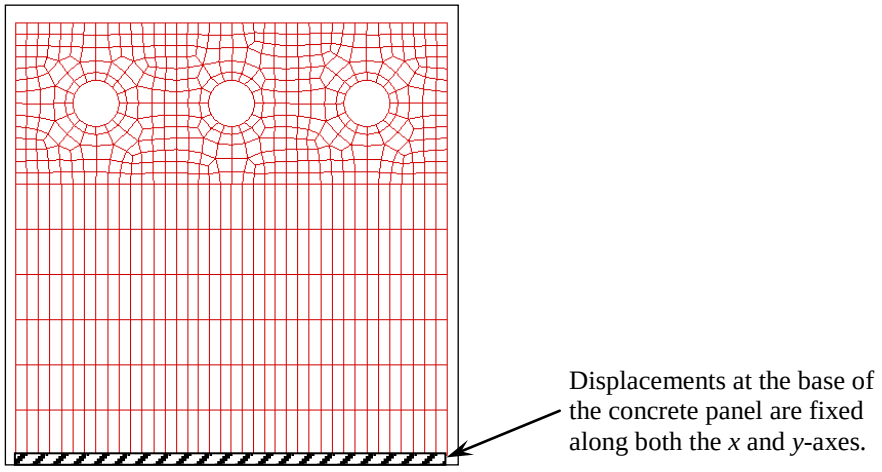

Figure 4: Finite element discretization of a reinforced concrete panel cross-section and imposed boundary conditions.

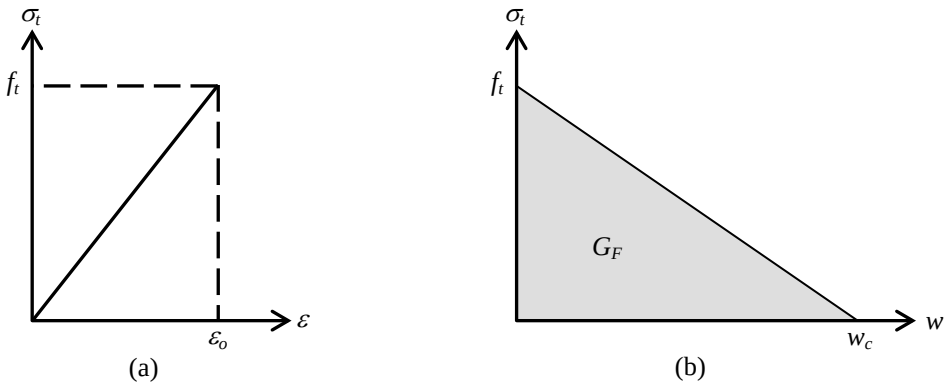

Figure 5: Concrete material model in tension: a) prior to cracking; b) tension softening relationship subsequent to crack formation.

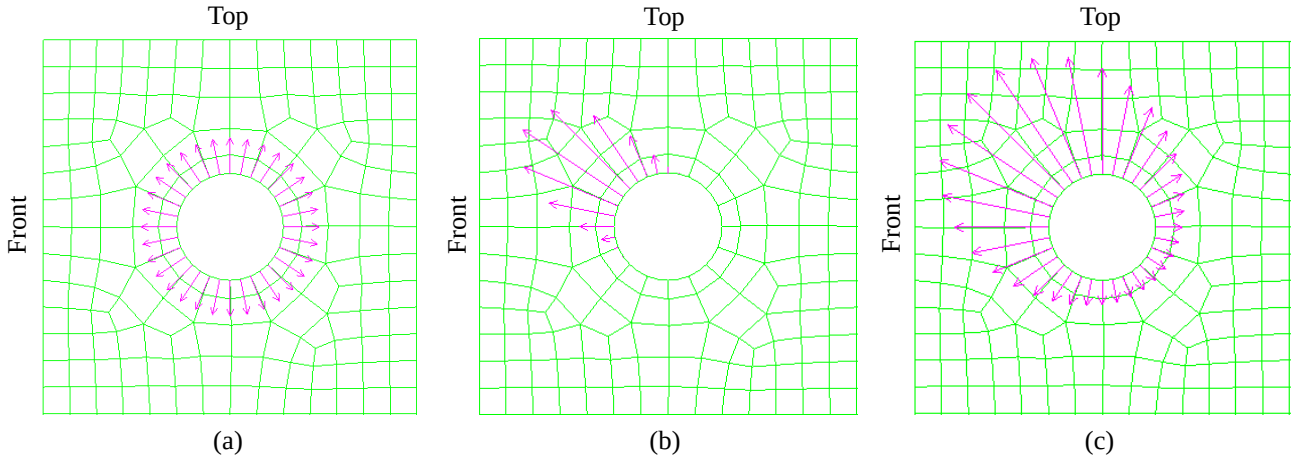

Figure 6: Corrosion scenarios modelled: a) uniform corrosion; b) uneven corrosion scenario (i); c) uneven corrosion scenario (ii).

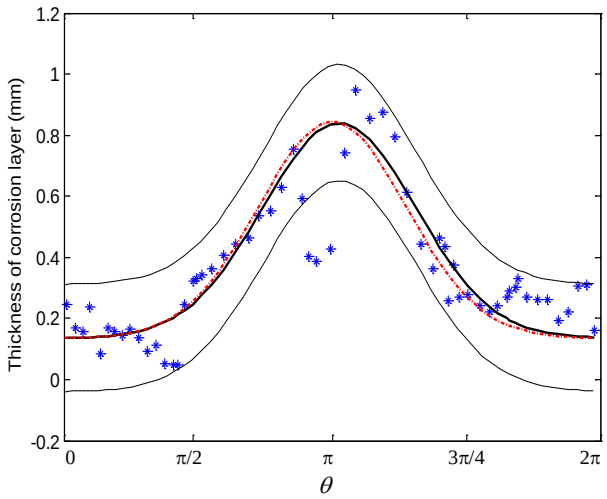

a) HPC-A-20 (Corrosion = 8.99%, Damage = 9%)

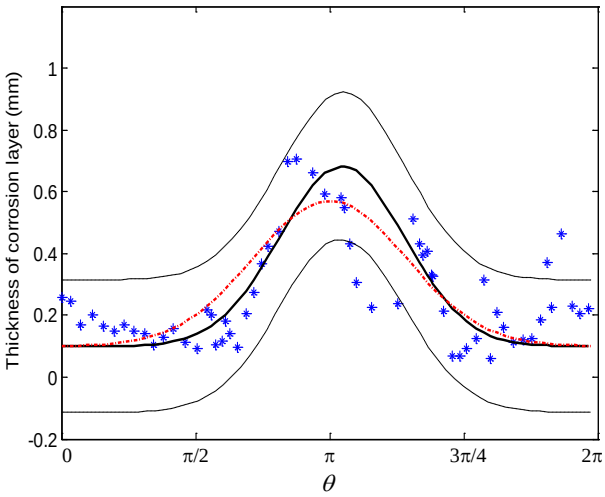

b) HPC-A-30 (Corrosion = 6.65%, Damage = 7.53%)

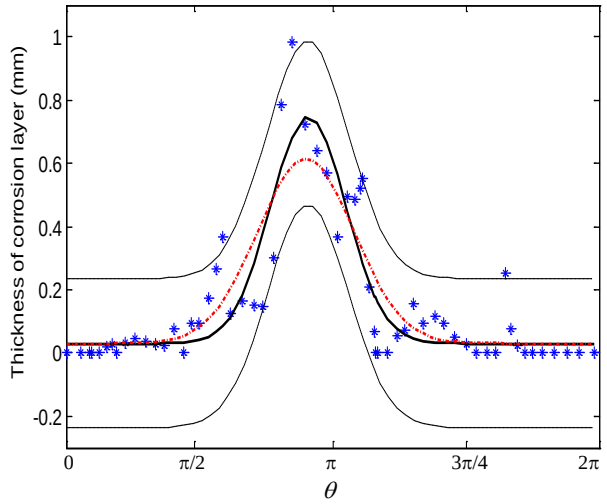

c) NC-B-20 (Corrosion = 4.61%, Damage = 5.76%)

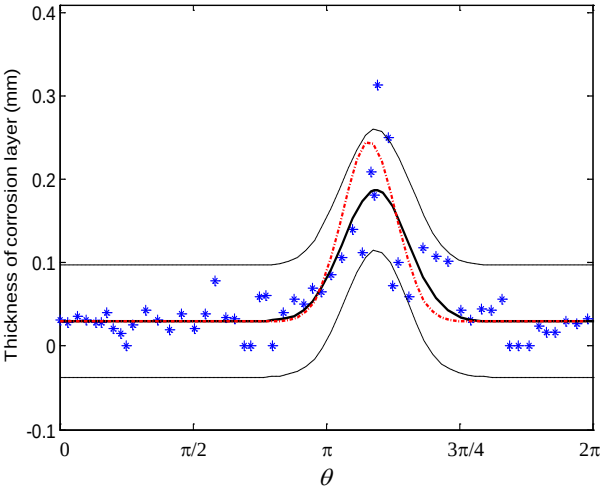

d) NC-B-30 (Corrosion = 2.97%, Damage = 2.61%)

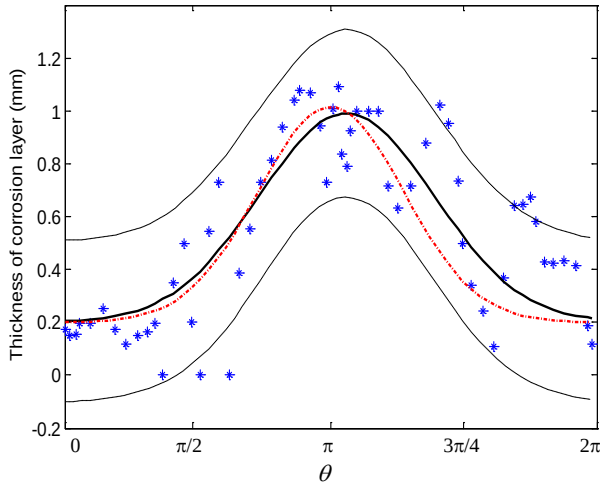

e) NC-A-10 (Corrosion = 8.47%, Damage = 13.81%)

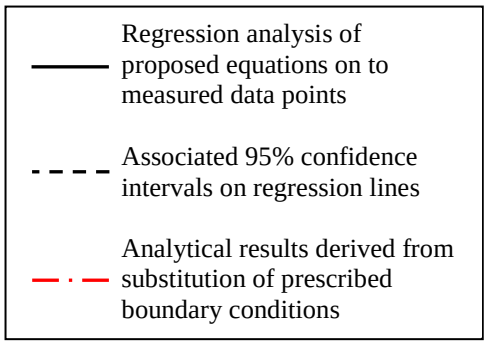

Figure 7: Measured thickness of corrosion layer around the rebar perimeter.

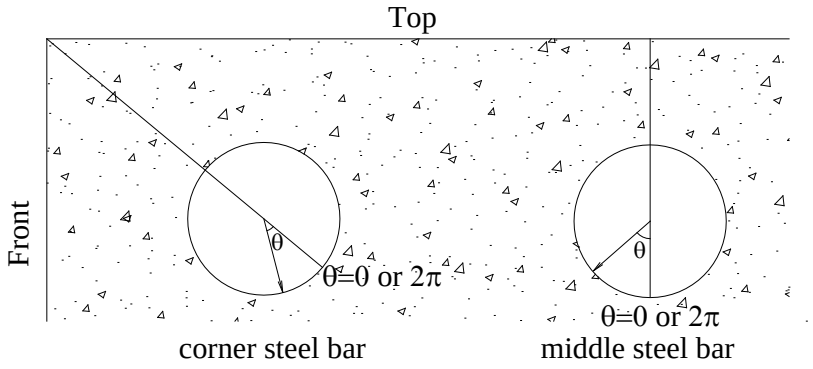

Figure 8: Polar coordinate system defined for the corner and middle rebar.

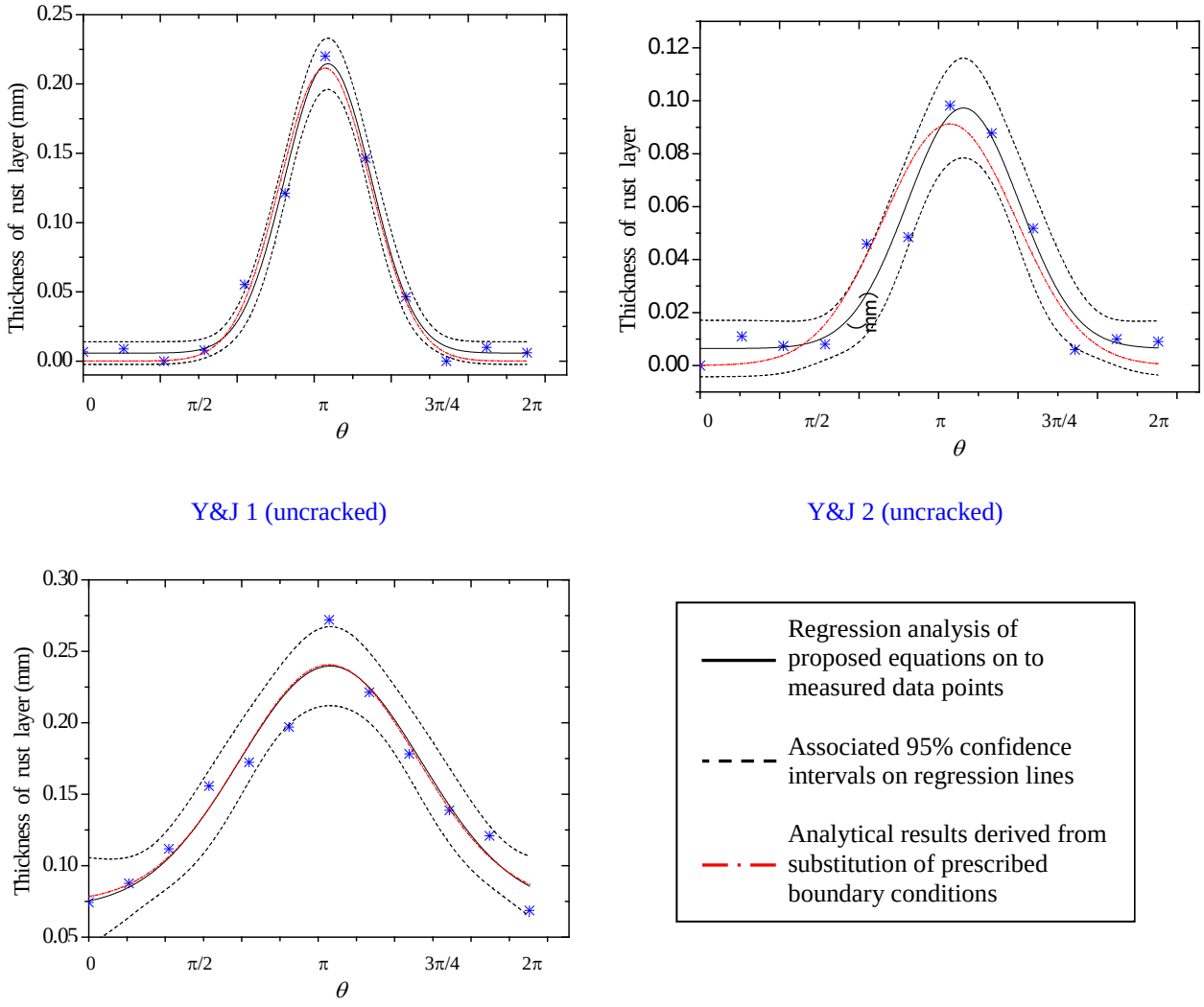

Fig.9 The regression analysis of the proposed Gaussian model on the data reported by Yuan and Ji

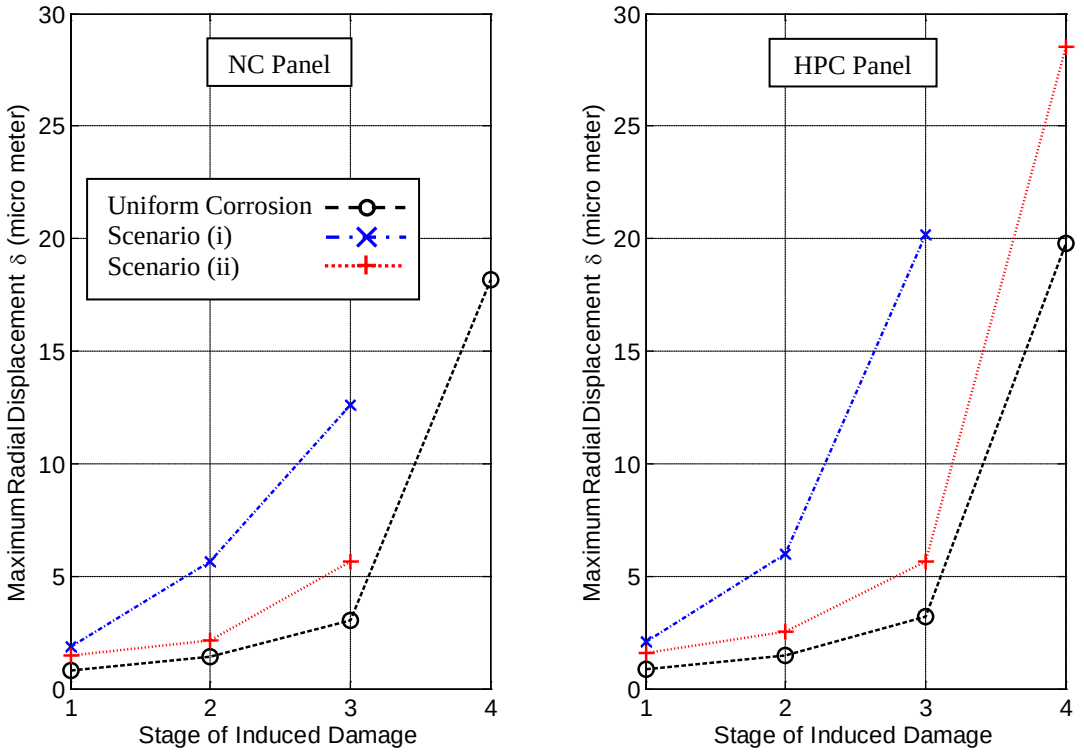

Figure 10: Maximum imposed radial displacements δ_{max} at varying stages of induced damage.

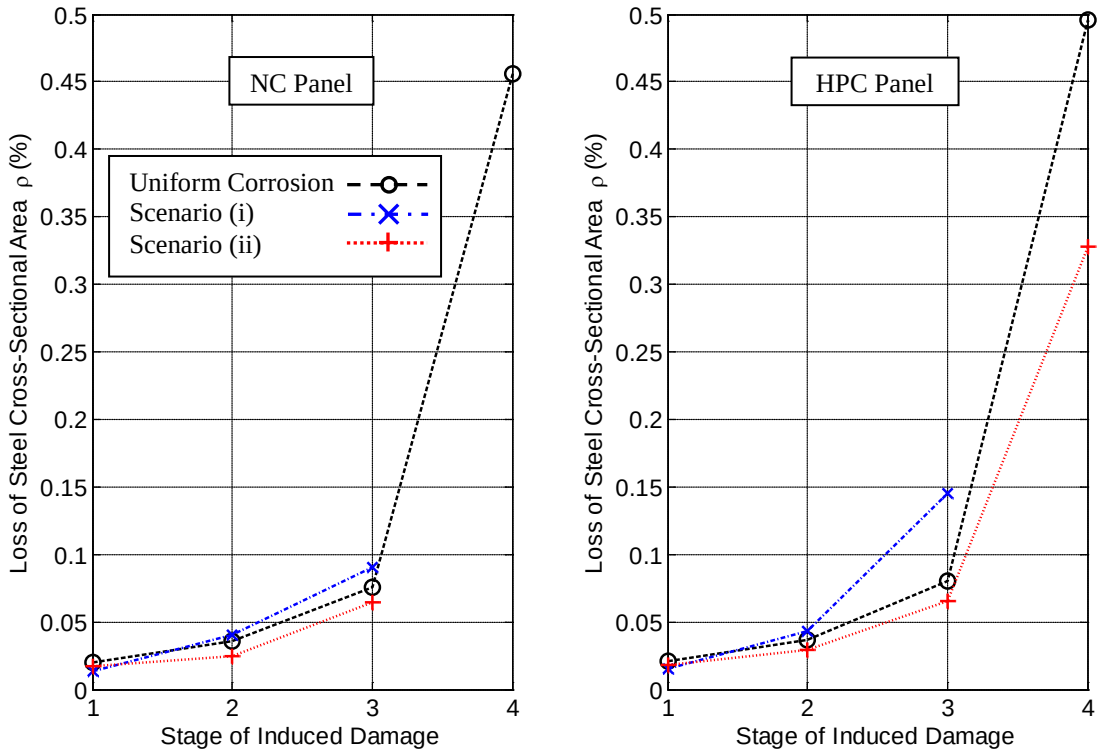

Figure11: Loss of steel cross-sectional area ρ at varying stages of induced damage.

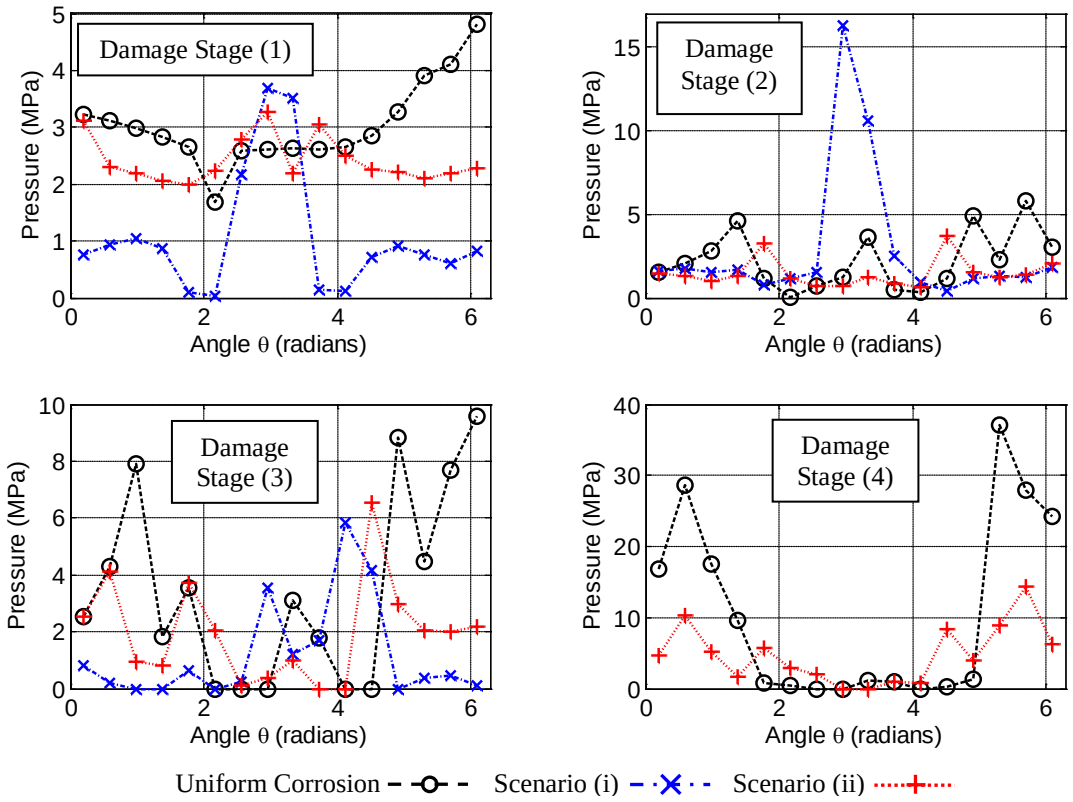

Figure 12: Pressure distribution around the reinforcement perimeter for all stages of damage for the HPC panel.

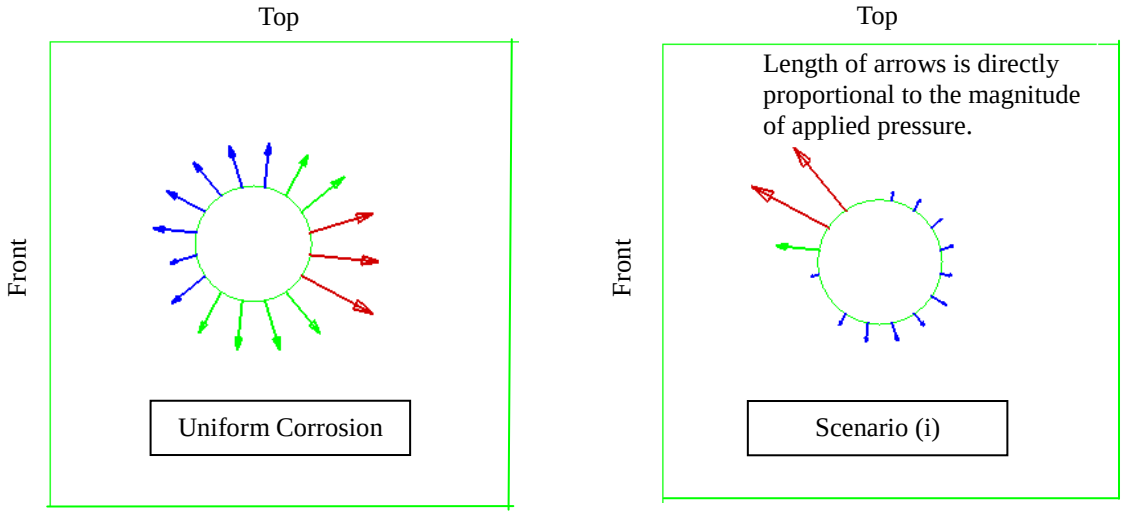

Figure 13: Pressure distribution around the reinforcement perimeter for the NC panel at damage stage (1) for uniform corrosion and scenario (i).

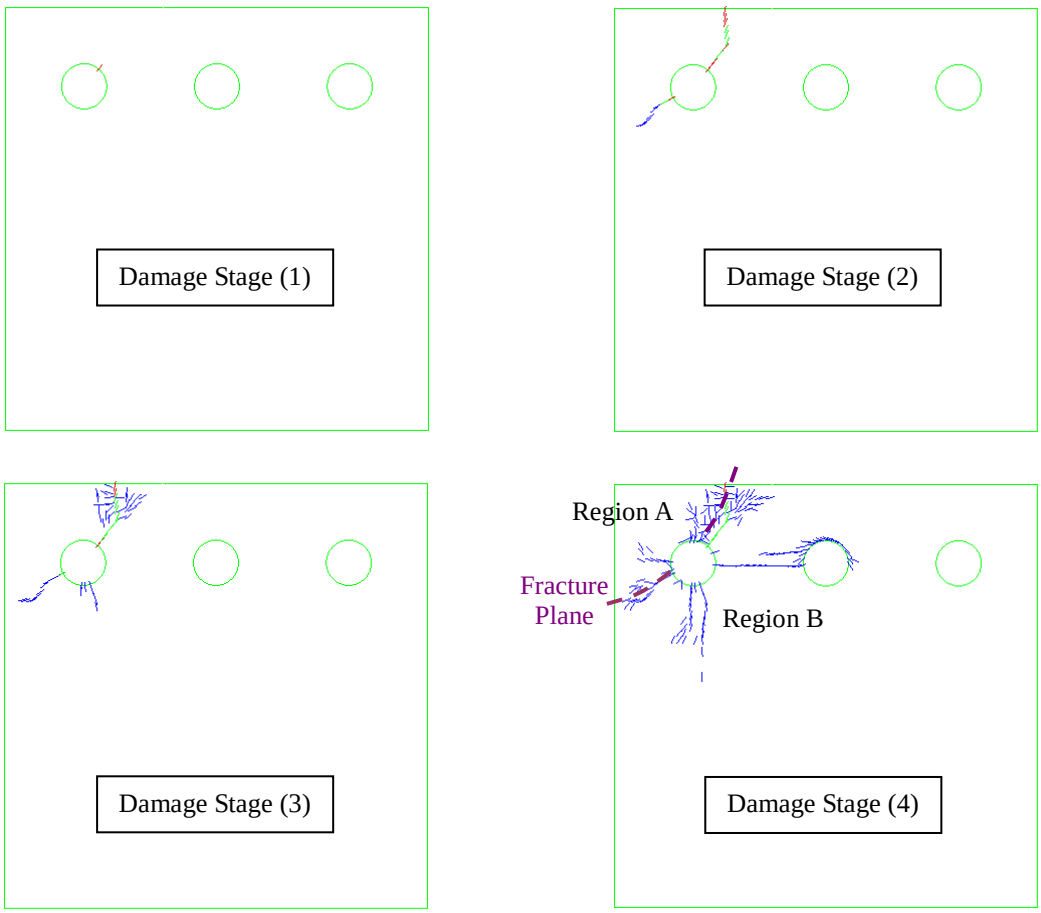

Figure 14: Evolution of the crack pattern from damage stage (1) to (4) for the HPC panel and scenario (ii).

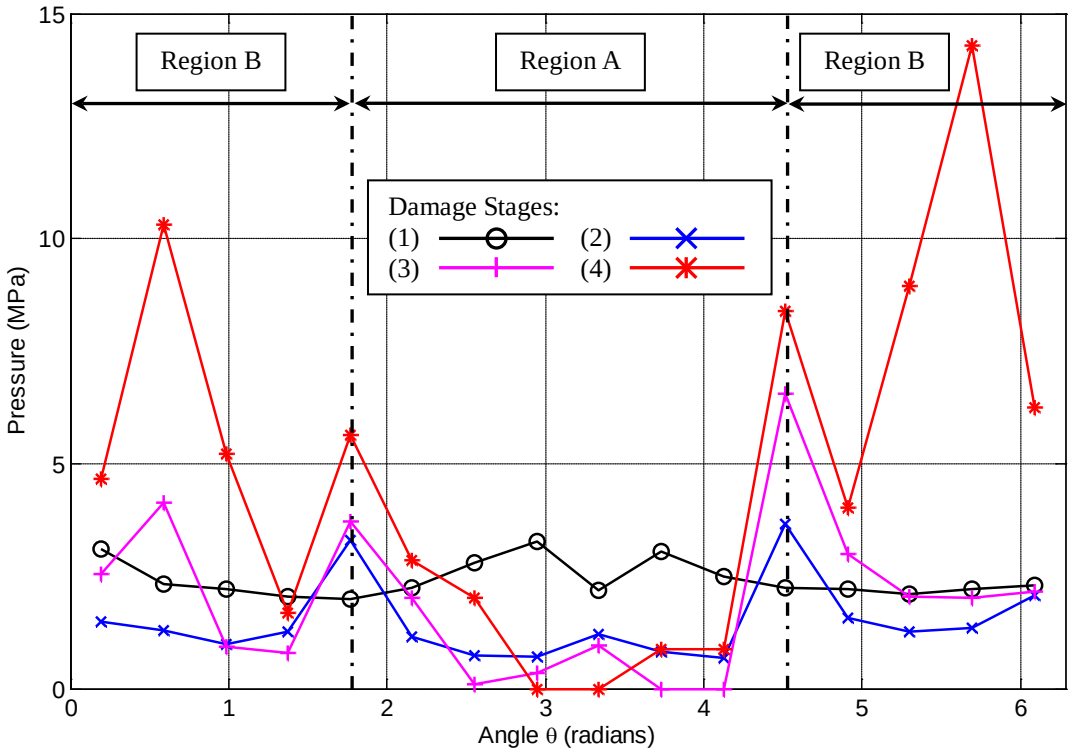

Figure 15: Pressure distribution around the reinforcement perimeter for the HPC panel and scenario (ii).